

See discussions, stats, and author profiles for this publication at: <https://www.researchgate.net/publication/272998930>

Formation of Titanium Nanostructures on Block Copolymer Templates with Varying Molecular Weights

ARTICLE in MACROMOLECULES · DECEMBER 2014

Impact Factor: 5.8 · DOI: 10.1021/ma501605s

READS

24

4 AUTHORS:



Martin Kreuzer

Catalan Institute of Nanoscience and Nanotec...

16 PUBLICATIONS 48 CITATIONS

[SEE PROFILE](#)



Claudia C. D. Simao

Eurecat

27 PUBLICATIONS 184 CITATIONS

[SEE PROFILE](#)



Ana Diaz

Paul Scherrer Institut

93 PUBLICATIONS 1,779 CITATIONS

[SEE PROFILE](#)



Clivia M. Sotomayor Torres

Catalan Institute of Nanoscience and Nanotec...

485 PUBLICATIONS 6,256 CITATIONS

[SEE PROFILE](#)

Formation of Titanium Nanostructures on Block Copolymer Templates with Varying Molecular Weights

Martin Kreuzer,^{*,†} Claudia Simão,[†] Ana Diaz,[‡] and Clivia M. Sotomayor Torres^{†,§}

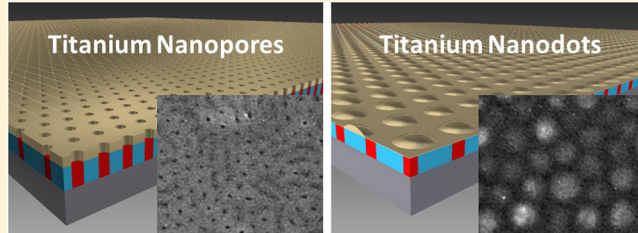
[†]Catalan Institute of Nanoscience and Nanotechnology (ICN2), Edifici ICN2, Campus UAB, 08193 Bellaterra, Spain

[‡]Paul Scherrer Institut, 5232 Villigen PSI, Switzerland

[§]Catalan Institute of Research and Advanced Studies (ICREA), 08010 Barcelona, Spain

Supporting Information

ABSTRACT: A novel and simple method for producing mesoporous titanium films and supported titanium nanoparticle hexagonal arrays is presented. During evaporation on block copolymer templates, titanium self-assembles as either a mesoporous film or as a hexagonal close-packed nanodot structure. The morphology of the titanium only depends on the molecular weight of the block copolymer, which results in a remarkable fabrication technique that saves time relative to conventional methods. Analyses using scanning electron microscopy, X-ray reflectometry, and grazing-incidence small-angle X-ray scattering correlate the morphology of the titanium with the buried polymer structure. The mesoporous titanium film exhibited a pore size of approximately 16 nm, with a pore-to-pore distance of 42 nm. The average size of the hexagonally packed nanodots was 60 nm, with a center-to-center distance of 88 nm commensurate with the template features. An analysis of the chemical composition showed that the structures were titanium dioxide, which indicated that oxidation occurred during the fabrication process.



Metal nanostructures have unique physical properties that are drastically different from the corresponding bulk material properties and result from the coupling of surface plasmons, excitons, or magnetic moments.¹ These unique properties include high dielectric constants,² wide energy band gaps,³ and high catalytic activity,⁴ which provide a wide functional diversity. Among others, titanium (Ti) nanostructures are used for electronic, optical, and sensor applications.⁵ These nanostructures exhibit a wide range of size-dependent properties that can be fine-tuned by controlling the architecture of the nanostructure.

To integrate nanostructures into practical applications, it is important to precisely control the alignment and size of the nanostructures on a substrate. The interactions between a template and nanoparticles result in a nanoparticle assembly that is predefined by the morphology, surface chemistry, and structure of the template. Recently, block copolymer (BCP) templates have attracted attention for preparing nanostructure arrays because they are facile and inexpensive.⁶ By using BCP self-assemblies, nanostructures with different morphologies and size distributions of between 10 and 100 nm can be obtained. These self-assembled nanostructures serve as templates for the fabrication of inorganic materials with structural features at the nanometre scale.^{7–9} Mesoporous metallic thin films,¹⁰ nanowires,¹¹ and nanodots⁷ have been prepared using functionalized BCP templates. In particular, hexagonal arrays of nanodots have received considerable attention in recent years.^{12,13} The main concept behind most of these studies is the selective decoration of one portion of the microphase-separated BCP templates

with an inorganic material.¹⁴ To achieve selective decoration, most preparation protocols require either functionalization^{9,10,12,15} or removal^{7,8,13,14} of portions of the BCP structure. Li et al. presented a method for fabricating hexagonally packed gold nanoparticles on electrically charged polymer templates by using Coulomb interactions,¹² which resulted in hexagonally packed particles with an average spacing (d) of 41 nm. Shin et al. used selectively etched polymer surfaces as templates for fabricating chromium and gold/chromium hexagonal arrays with an average spacing of 34 nm.⁷

Metallic nanowires for industrial-scale manufacturing have been produced using the thermal evaporation method.¹⁶ Evaporated metal particles arrange selectively on phase-separated BCP templates after additional annealing steps.¹¹ The intrinsic difference in the surface chemistry between the two phase-separated units of a BCP film is used for the selective decoration of the BCP template. The resulting metal structures depend strongly on the metal/BCP combination.^{17–19} The preparation protocol, the choice of metal and the combination of the monomer units in a BCP are crucial for the resulting Ti formation.¹⁷ However, to the best of our knowledge, differences in metal formation on only one type of BCP have not been previously observed.

In this study, we present the decoration of unaltered polystyrene-*b*-poly(ethylene oxide) (PS-*b*-PEO) BCP templates

Received: August 4, 2014

Revised: October 31, 2014

Published: December 12, 2014

by Ti nanoparticles. This is the first study to investigate the differences in Ti formation on PS-*b*-PEO surfaces that differ only in their molecular weight ratios. Our results reveal an unexplored difference in the formation of Ti on surfaces that are chemically identical. This preparation method avoids the use of etching steps and does not rely on subsequent annealing processes. Local information regarding the sample surface was obtained using scanning electron microscopy (SEM). In addition, the nondestructive characterization of large sample areas to acquire in-depth information was performed using grazing-incidence small-angle X-ray scattering²⁰ (GISAXS) and X-ray reflectometry²¹ (XRR) measurements.

RESULTS AND DISCUSSION

Structural and Dimensional Characterization of the Polymer Templates. To study the formation of Ti on BCP templates with varying molecular weights, two different BCP templates, A and B, were prepared. Here, two different PS-*b*-PEO polymers with different molecular weights were chosen for dimensional control over the templated nanostructures. For template A, a solution of PS-*b*-PEO with molecular weights of $M_{n,PS} = 42$ kg/mol and $M_{n,PEO} = 12$ kg/mol (42 k–12 k) was used. For template B, a solution of PS-*b*-PEO with molecular weights of $M_{n,PS} = 102$ kg/mol and $M_{n,PEO} = 34$ kg/mol (102 k–34 k) was used. Figure 1 presents the SEM images of the samples. The measured surface area was $1.9 \mu\text{m}^2$. The microphase separation of the BCPs resulted in the formation

of PEO cylinders (shown in black) in the PS matrix (shown in gray). The two templates differ in terms of their cylinder radius R and the average spacing d between the cylinders, which resulted from the different chain lengths of the two BCPs. As reported elsewhere, higher molecular weight BCPs have longer chains, which result in larger cylinder radii and larger spacings between the components of the same phase.¹³

Most of the surface of template A is covered with vertically oriented cylinders (Figure 1a). The cylinders have a radius of $R = 8 \pm 2$ nm, with a center-to-center spacing of $d = 40 \pm 5$ nm. Some areas show linear features, which are PEO cylinders that are aligned parallel to the substrate. One example is highlighted by a dotted white ellipse in Figure 1a. In contrast, template B only shows vertically aligned PEO cylinders with $R = 13 \pm 2$ nm and $d = 100 \pm 10$ nm (Figure 1b). The estimated radii and spacings of the BCP templates are listed in Table 1. Information regarding the in-plane domain orientation along the sample surface over a substantially larger lateral area than afforded by SEM was obtained using GISAXS measurements. Figure 2 (a, b) presents the measured 2D GISAXS intensity patterns. The small difference in the densities of the microphase-separated PS and PEO within the BCP film was sufficient to obtain a measurable X-ray scattering contrast.²²

As indicated by the dashed vertical white lines in Figure 2a,b, first-order diffraction peaks were observed on both sides of the beamstop at $Q_{y,\max} = \pm 0.171 \text{ nm}^{-1}$ and $Q_{y,\max} = \pm 0.078 \text{ nm}^{-1}$ for templates A and B, respectively. The diffraction peaks in the GISAXS patterns resulted from the vertically aligned PEO cylinders in the PS matrix over a large sample area.

Horizontal line cuts were analyzed in a detailed study on the in-plane sample geometries. Figure 3a shows these horizontal cuts of the 2D GISAXS pattern that were integrated over a finite Q_z -range with the center at $Q_z = 0.36 \text{ nm}^{-1}$ (where the scattering spots appear). The integrated areas are indicated with red rectangles in Figure 2a,b. In addition to the first-order diffraction peak, a second-order peak is visible at $Q_{y,\max} = 0.30 \text{ nm}^{-1}$ and $Q_{y,\max} = 0.14 \text{ nm}^{-1}$ for templates A and B, respectively. The second-order peak, which appears at a relative distance of $\sqrt{3}$ from the first-order peak, confirms that the oriented cylinders are arranged in a hexagonal lattice on the sample surfaces. Fits to the data were conducted using the IsGISAXS software package.²³ The scattering profiles were fit using the distorted-wave Born approximation for supported islands on a silicon substrate and the decoupling approximation. The best agreement with the experimental profiles was obtained by assuming a cylindrical particle shape and using the isotropic interference function for hexagonal symmetry. The fitting parameters included the cylinder radius R , the relative width of the radius distribution σ_R , the average cylinder center-to-center spacing d , and the relative width of the Gaussian distribution σ_d that was used in the pair correlation function. The resulting fitting parameters are listed in Table 2.

The first-order diffraction peak for template B appeared at very low Q_y values and is superimposed on the strong scattering signal of the specular plane ($Q_y = 0$). Therefore, it was not possible to fit the entire peak and smaller Q_y values could not be considered for the fitting routine. Nevertheless, the resulting radii of 9 and 12 nm and the d spacings of 42 and 88 nm for templates A and B, respectively, agree with the SEM data.

Regarding the out-of-plane structure, the 2D GISAXS maps provide information in the vertical direction of the samples (Figure 2a,b). Here, the diffraction peaks have two distinct maxima, which correspond to two characteristic Q_z values that

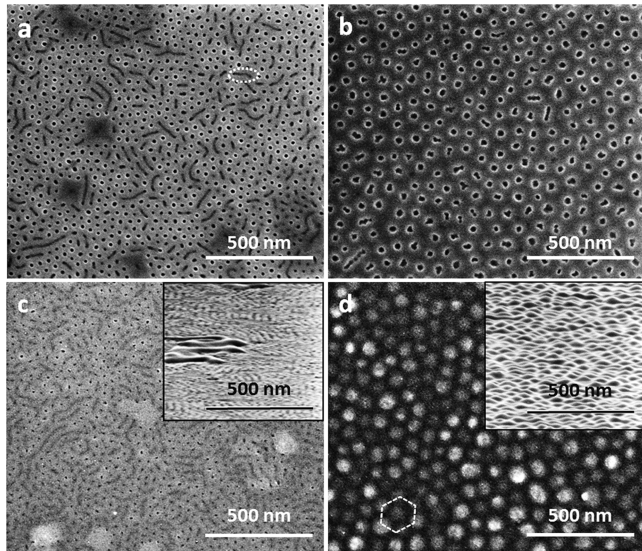


Figure 1. SEM images of the prepared BCP templates (a, b) and the templates with the nominal Ti coatings of 10 nm (c, d). In the top row, the as-spun PS-*b*-PEO BCP templates with molecular weights of 42k–12k (a) and 102k–34k (b) are shown. The lighter areas represent the PS and the darker areas represent the PEO of the microphase-separated PS-*b*-PEO BCPs. A horizontally aligned PEO cylinder is highlighted by a white ellipse in a. The bottom row shows images of the sample surfaces of the BCP templates with molecular weights of 42k–12k (c) and 102k–34k (d) after the evaporation of a nominal Ti amount of 10 nm, which appears in lighter shades of gray. A hexagonal structure is highlighted by a white hexagon in part d. The insets in parts c and d show tilted views (80°) of the corresponding samples. All scale bars correspond to 500 nm. The samples in images c and d are denoted C and D and are discussed in the Mesoporous Titanium Film and Titanium Nanodot Array sections, respectively.

Table 1. Summary of the Prepared Samples Used in This Study^a

	sample label			
	A	B	C	D
$M_{n,PS} - M_{n,PEO}$ [g/mol]	42k–12k	102k–34k	42k–12k	102k–34k
coating	—	—	10 nm Ti	10 nm Ti
R [nm]	8 ± 2	13 ± 2	4 ± 1	38 ± 3
d [nm]	40 ± 5	100 ± 10	40 ± 5	100 ± 10

^a M_n is the molecular weight of the respective PS and PEO components of the BCPs. R is the radius and d is the average center-to-center distance between the PEO cylinders embedded in the PS matrix which was estimated from the SEM micrographs before and after the evaporation of 10 nm titanium (Ti) (see Figure 1). Samples C and D are discussed in the Mesoporous Titanium Film and Titanium Nanodot Array sections, respectively.

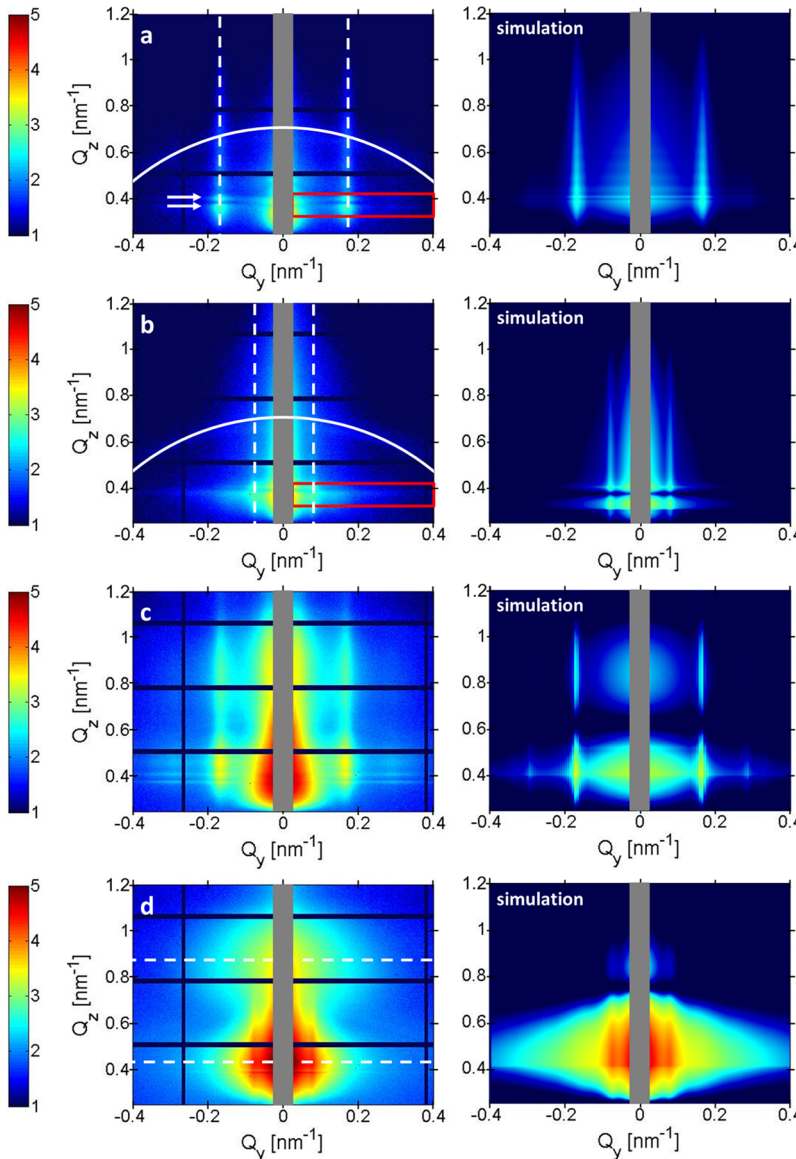


Figure 2. 2D GISAXS intensity patterns of the prepared BCP templates, A (shown in part a) and B (shown in part b), and the templates with nominal Ti coatings of 10 nm (shown in parts c and d). The arrows in part a indicate the critical angles of the silicon substrate and the BCP thin film. The white arcs indicate scattering from the windows of the evacuated beam path. The first-order positions of the scattering signals are marked by vertical dashed lines in parts a and b. The formation of the Ti film could be observed as maxima in the z-direction, as indicated by the horizontal lines in part d. Corresponding simulations are displayed in the right column and the intensities are shown on a logarithmic scale. The areas of the beamstops are indicated by the gray boxes around $Q_y = 0$.

are marked by two white arrows in Figure 2a. In this case, the maxima corresponds to the Yoneda wings of the reflecting surfaces of the samples, and appear at the critical angles of reflection α_c for the PS-*b*-PEO and the buried silicon surface.²⁴

The horizontal intensity line at a constant $Q_z = 0.40 \text{ nm}^{-1}$ corresponds to a critical angle α_c of 0.15° , which was extracted from equation 2 with $\alpha_i = 0.25^\circ$ and agrees with the expected critical angle of silicon at the energy used in the experiment

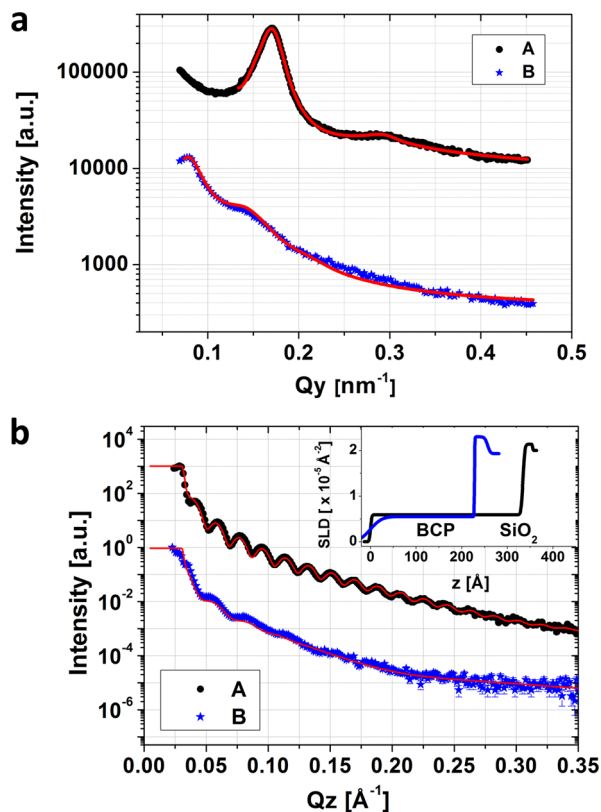


Figure 3. (a) Horizontal cuts of the 2D GISAXS pattern of templates A and B around a finite Q_z range centered at $Q_z = 0.36 \text{ nm}^{-1}$. The integrated areas are shown with red rectangles in Figure 2a,b. (b) XRR data of templates A and B. Full black dots correspond to template A, which is the BCP with a molecular weight of 42 k-12 k, and the blue stars correspond to template B, which is the BCP with a molecular weight of 102 k-34 k. The red lines are fit to the data and the data points are shifted vertically for clarity. The resulting scattering length density (SLD) profiles are shown in the inset to part b in units of 10^{-5} \AA^{-2} versus the sample depth z . The black (blue) line corresponds to template A (B).

Table 2. Fitting Parameters for the Horizontal Cuts of the GISAXS Pattern^a

sample	A: 42 k-12 k	B: 102 k-34 k	C: 42 k-12k + 10 nm Ti	D: 102 k-34k + 10 nm Ti
radius R [nm]	9	12	8	30
σ_R [nm]	0.50	0.36	0.73	0.25
d spacing [nm]	42	88	44	80
σ_d [nm]	3	15	2	20
aspect ratio H/R	3.75	1.30	1.40	0.50
$\sigma_{H/R}$	0.33	0	0.001	0.15

^aCylinder radius R , the relative width of the radius distribution σ_R , the average cylinder center-to-center d spacing, the relative width of the Gaussian distribution used in the pair correlation function σ_d , the cylinder aspect ratio H/R , and the relative width of its distribution function $\sigma_{H/R}$. The corresponding line fits are shown in Figure 3a, and the 2D simulations are shown in Figure 2 (right column).

($\alpha_c(\text{Si}) = 0.16^\circ$).²⁵ The maximum at the lower Q_z values was observed at 0.37 nm^{-1} , which corresponds to a critical angle of 0.12° and is comparable to the reported critical angle of $\alpha_c(\text{PS-PEO}) = 0.14^\circ$ for PS-*b*-PEO indicating the formation of a

continuous polymer film on the silicon substrate.^{22,26} The experimentally obtained 2D GISAXS pattern was simulated by using the same IsGISAXS software package with the parameters extracted from the line fitting, the cylinder aspect ratio H/R and the relative width of its distribution function $\sigma_{H/R}$. The distorted-wave Born approximation for holes in a layer on a silicon substrate was used for this simulation. The results are shown in Figure 2 (right column). The main characteristics, the radii R and the average spacings of the PEO cylinders (d), agreed with the results that were predicted by the simulation. The intensities parallel to the sample surfaces, which are referred to as the Yoneda wings, could also be reproduced by the simulation. The results indicated that a hexagonal arrangement of vertically aligned cylinders was present on the sample surface at a macroscopic scale. The driving force for the BCP self-assembly results from the immiscibility of the two polymer chains of the BCP molecules.²⁷⁻³⁰

To obtain more detailed information regarding the out-of-plane structures perpendicular to the sample surface, templates A and B were investigated using XRR. The measurements and corresponding data fits are shown in Figure 3b. Kiessig oscillations are observed due to the differences in scattering length densities between the silicon substrate and the thin BCP films.³¹ The frequency is proportional to the BCP layer thickness, while the intensity amplitudes are influenced by the scattering contrast and surface roughness. To fit the data using the MOTOFIT software package,³² the film was modeled using two consecutive layers on a silicon substrate (Si), a BCP layer and a silicon dioxide (SiO_2) layer. For each layer, the thickness (t), roughness (δ), and scattering length density (SLD) were varied until the best fit was achieved according to the minimum χ^2 value. The resulting parameters are listed in Table 3. The calculations revealed that template A has a smoother surface than template B, with BCP surface roughness of 0.2 and of 2.0 nm. Layer thickness was 33.4 and 22.8 nm for templates A and B, respectively. The difference in the layer thickness is attributed to the differences in the molecular concentrations in the solutions during the preparation of templates A and B.³⁰ The calculated SLDs for Si, SiO_2 , and BCP all agreed with the theoretical values³³ and are shown with their corresponding layer thickness in Figure 3b (inset).

In summary, BCP templates were prepared that were composed of hexagonally ordered PEO cylinders in PS matrices. These templates were used to study the formation of Ti on BCP thin films with two different molecular weights that have the same surface chemistry but exhibit different PEO cylinder radii and center-to-center spacings.

Mesoporous Titanium Film. The evaporation of a small amount of Ti on template A does not lead to a continuous Ti layer. Instead, the SEM image of sample C shows that Ti selectively covers the PS portion of the BCP surface (Figure 1c). Even after the evaporation of Ti with a nominal layer thickness of 10 nm, the PEO cylinders are still distinguishable in black. The pores in the Ti layer have a radius of approximately $4.0 \pm 0.5 \text{ nm}$, which is approximately 2 nm smaller than the radius of the polymer cylinders. The estimated spacing between the pores in the Ti layer and the polymer cylinders are practically identical at approximately $40 \pm 5 \text{ nm}$. All values are listed in Table 1. A cross section TEM image is shown in Figure 5a. The picture shows a covering Ti layer with a thickness of approximately $14 \pm 2 \text{ nm}$ on a BCP film with a thickness of $11 \pm 3 \text{ nm}$. Because of the nonplanar surface the exact thickness of the BCP and the Ti film cannot be extracted

Table 3. Fitting Parameters for the XRR Profiles, Including the Layer Thickness t , Roughness δ , and Scattering Length Density SLD^a

layer	sample											
	A: 42k–12 k			B: 102k–34 k			C: 42k–12k + 10 nm Ti			D: 102k–34k + 10 nm Ti		
	t [nm]	δ [nm]	SLD ^b	t [nm]	δ [nm]	SLD ^b	t [nm]	δ [nm]	SLD ^b	t [nm]	δ [nm]	SLD ^b
air	N/A	—	0	N/A	—	0	N/A	—	0	N/A	—	0
dots	—	—	—	—	—	—	—	—	—	11.5	2.4	3.1
TiO ₂	—	—	—	—	—	—	11.2	1.4	3.4	1.8	1.3	3.4
Ti	—	—	—	—	—	—	4.0	0.3	3.5	0.2	0.8	3.5
BCP ^c	33.4	0.2	0.6	22.8	2.0	0.7	32.2	1.3	1.2	18.9	2.0	1.2
SiO ₂	2.1	0.3	2.1	2.9	0.1	2.3	2.0	0.3	2.1	2.0	0.4	2.2
Si	N/A	0.1	2.0	N/A	0.5	1.9	N/A	0.5	2.0	N/A	0.4	2.0
χ^2		0.01			0.04				0.02		0.02	

^aThe fits are shown in Figure 3b and 4a. The information regarding the thickness of the silicon substrate and the air surrounding the substrate is not applicable (N/A). ^bSLD is given in units of 10^{-5} \AA^{-2} . ^cBCP represents the PS-*b*-PEO BCP layer.

from the measurements, as the profile of the Ti film appears thicker in the measured cross section slice, having a finite thickness of several micrometers in electron beam direction. PEO cylinders are not visible, due to the low contrast between PS and PEO. Furthermore, the pores could not be resolved in the covering Ti film as the pore diameter is much smaller than the thickness of the measured sample slice.

The GISAXS pattern of template A changed drastically upon the evaporation of the Ti. The 2D intensity map of sample C is shown in Figure 2c. The overall scattering intensity of the sample was enhanced due to the higher SLD of Ti. In addition to the background level, the diffuse scattering near the specular reflection plane and the intensities along the diffraction peak in the Q_z direction drastically increase. The Yoneda wing, with a maximum intensity at $Q_z = 0.46 \text{ nm}^{-1}$, corresponds to the critical angle of Ti at $\alpha_c(\text{Ti}) = 0.22^\circ$.³⁴ The 2D GISAXS scattering pattern could be simulated using the pore radius R, d spacing and H/R aspect ratio as parameters. All parameters are listed in Table 2.

The in-plane scattering signal shows maxima to the left and right of the specular intensity at $Q_y = \pm 0.167 \text{ nm}^{-1}$. These characteristic scattering signals clearly indicate a correlation between the underlying polymer template and the mesoporous Ti film because they appear at the same Q_y values. Therefore, we conclude that the spacing of the underlying PEO polymer cylinders determines the spacing of the pores in the Ti film. Moreover, a maximum along the diffraction peak in the vertical direction appears at higher Q_z values, with $Q_{z,\max} = 0.85 \text{ nm}^{-1}$. The Ti layer results in regular intensity oscillations along Q_z . These Kiessig oscillations are generally measured in XRR experiments and are discussed in the following section.

XRR measurements were performed to obtain detailed information about the formation of the Ti layer (Figure 4a). For data fitting, the total film was modeled with a four-layer model on a silicon substrate with titanium dioxide (TiO₂), titanium (Ti), BCP, and silicon oxide (SiO₂) layers. A schematic illustration of the modeled layer system is shown in Figure 4b. The corresponding calculated SLD profiles are shown in the inset to Figure 4a. The data analysis shows the formation of an 11.2 nm thick TiO₂ layer with an SLD of $3.4 \times 10^{-5} \text{ \AA}^{-2}$. Below the upper TiO₂ layer, a layer of metallic Ti with a thickness of 4.0 nm and a SLD of $3.5 \times 10^{-5} \text{ \AA}^{-2}$ appears. The high peak between $z = 0$ and 100 Å that results from the high SLD of Ti and TiO₂ is particularly evident. These

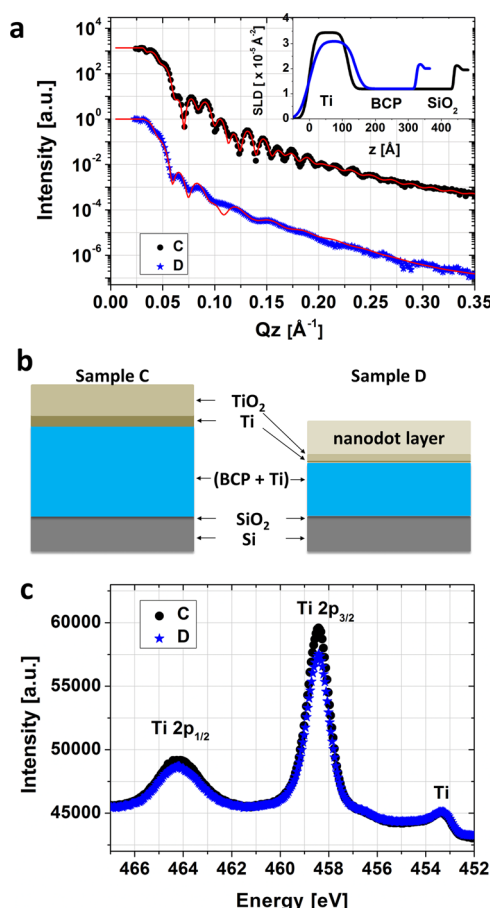


Figure 4. (a) XRR data of the Ti-coated BCP templates. The full black dots correspond to sample C, with a BCP molecular weight of 42k–12k and the blue stars correspond to sample D with a BCP molecular weight of 102k–34k after the evaporation of Ti. The red lines are fit to the data and the data points are shifted vertically for clarity. The resulting scattering length density (SLD) profiles are shown in the inset in units of 10^{-5} \AA^{-2} against the sample depth z, and the black and blue lines corresponds to samples C and D, respectively. (b) Schematics of the layers used in the fitting routine for sample C and sample D. (c) XPS spectrum of the mesoporous thin film (sample C) and the nanodot structure (sample D). The two peaks at 464.2 and 458.3 eV are typically attributed to TiO₂. The smaller peak at 453.3 eV indicates the presence of metallic Ti.

results agree with the chemical composition analyses of the sample surface, which indicated the formation of TiO_2 and Ti and are discussed later. The experimental XRR data and the corresponding fits are shown in Figure 4a and are listed in Table 3 (column C).

In addition, the XRR analysis shows an increase in the scattering length density of the BCP layer after the evaporation of the Ti. Before evaporation, the BCP layer has a calculated SLD of $0.6 \times 10^{-5} \text{ \AA}^{-2}$, which is lower than the theoretical value of a close-packed layer of PS-*b*-PEO with a SLD of $0.9 \times 10^{-5} \text{ \AA}^{-2}$. After evaporation, the layer was best fit with a SLD of $1.2 \times 10^{-5} \text{ \AA}^{-2}$. The increase in the SLD of the BCP layer can be explained by the diffusion of the Ti particles into the polymer matrix. Metwalli et al. reported a similar effect for gold particles sputtered on a BCP template, which diffused into the polymer template.³⁵ The increase in SLD is due to the high scattering length density of the Ti with $3.5 \times 10^{-5} \text{ \AA}^{-2}$. The increase in the SLD of $0.6 \times 10^{-5} \text{ \AA}^{-2}$ for the BCP layer corresponds to a volume portion ϕ of 21% Ti in the BCP layer when using equation 1.³⁶

$$\phi(\text{Ti}) = \frac{\text{SLD}(\text{BCP layer after evap}) - \text{SLD}(\text{BCP layer before evap})}{\text{SLD}(\text{Ti}) - \text{SLD}(\text{BCP layer before evap})} \quad (1)$$

Here, we assume that the BCP layer thickness does not change upon the evaporation of Ti. The measurements do not reveal whether Ti is embedded in the PS or the PEO portion of the BCP layer. Our results suggest that the accumulation of Ti is not limited to the flat polymer surface but also permeates the matrix of the insulating polymer bulk material.

The chemical composition analysis of the Ti texture on the sample surface by XPS is shown in Figure 4c. The peaks at

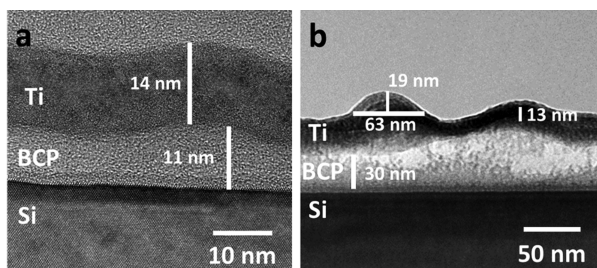


Figure 5. TEM cross sections of titanium (Ti) mesoporous film (a) and Ti nanodots (b) on block copolymer (BCP) templates on silicon (Si) substrates.

459.1 and 463.9 eV correspond to Ti $2p_{3/2}$ and Ti $2p_{1/2}$, respectively, and demonstrate the formation of TiO_2 . The lowest energy peak at 453.3 eV is associated with metallic Ti.³⁷

A mesoporous Ti/ TiO_2 film could be prepared with a hexagonal array of nanoholes. A sketch is shown in Figure 6a. Furthermore, the diffusion of Ti nanoparticles into the BCP template was observed, which indicates the possibility of accumulating isolated Ti nanoparticles in a polymer film.

Titanium Nanodot Array. Upon the evaporation of Ti on template B, a hexagonally packed Ti nanodot structure emerged (see Figure 1d) that was distinct from the mesoporous film of sample C. Images of sample D show nanodots with an estimated radius of 38 ± 3 nm and a spacing of 100 ± 10 nm. SEM images of the sample surface under a tilt angle of 80° reveal an estimated height of 12 ± 3 nm (inset to Figure 1d). A

TEM cross-section image of the sample is shown in Figure 5b and reveals a height of 19 ± 2 nm with a radius of 32 ± 2 nm of a single nanodot on a 13 ± 2 nm thick Ti layer. The BCP template had a thickness that varied between 20 and 40 nm. These variations are due to the nonplanar surface morphology of the Ti film, as revealed by TEM images. The nonplanar surface is due to the spin coating inhomogeneity and particle defects.

A large area of sample D could be probed using GISAXS experiments (Figure 2d). As observed for the mesoporous Ti film, the addition of Ti drastically increases the scattering signal around the specular reflection signal. The in-plane scattering signal shows a pronounced peak at $Q_y = \pm 0.077 \text{ nm}^{-1}$, which is only shifted by 0.001 nm^{-1} from the Q_y value of the in-plane signal of the pure polymer template B. The congruence of the resulting Q_y values underlines the strong correlation between the nanodot structure and the underlying BCP structure. The best simulation of the data was achieved by modeling the cylinders in a hexagonal arrangement with a radius R of 30 nm, a center-to-center distance of 80 nm and relative Gaussian distributions of $\sigma_R = 0.25 \text{ nm}$ and $\sigma_d = 0.25 \text{ nm}$. An aspect ratio of $H/R = 0.5$ with a relative distribution of $\sigma_{H/R} = 0.15$ provided the best results. Along the vertical direction, the first maximum appears at $Q_z = 0.43 \text{ nm}^{-1}$ and the second maximum appears at $Q_z = 0.86 \text{ nm}^{-1}$, as indicated by the two dashed horizontal lines in Figure 2d. These regular oscillations along Q_z can be explained by the formation of a Ti layer. A layer thickness of 14.6 nm was obtained by using the Bragg equation with $d = 2\pi/\Delta Q_{z,\max}$.

The structure of the sample in the z -direction, i.e., in the direction of the sample normal, could be solved in detail by XRR measurements (Figure 4a). The frequency of the Kiessig oscillations is higher than of the uncoated polymer template B due to the formation of an additional layer on the substrate. The experimental results were simulated using a box model layer system of the sample. A five-layer system of nanodots (dots), titanium dioxide (TiO_2), titanium (Ti), BCP and silicon oxide (SiO_2) provided the best fit to the data. The thickness (t), SLD and roughness (δ) of each layer were varied until the best fit was achieved. In this model, the nanodots were represented by an extra layer. A schematic illustration of the modeled layer system is shown in Figure 4b. The calculations revealed that the BCP film is covered by thin films of TiO_2 and Ti with thickness of 1.8 and 0.2 nm, respectively. The calculated SLD profile is shown in the inset to Figure 4a. The nanodots appear with an effective SLD of $3.1 \times 10^{-5} \text{ \AA}^{-2}$, which is smaller than the expected value of $3.4 \times 10^{-5} \text{ \AA}^{-2}$ for TiO_2 because the TiO_2 density in the nanodot layer is considerably lower than that in a homogeneous layer. Furthermore, the calculations revealed that 18% of the BCP layer volume was occupied by diffused Ti particles. The XPS chemical analysis revealed that the chemical composition was similar to the mesoporous Ti coating (Figure 4c) and indicated that the outer surface of the metal film (5–6 nm) consist to 90% of TiO_2 .

These results show that the hexagonal BCP template structure is reproduced by the Ti coating, as schematically shown in Figure 6b. The metal coating forms hexagonally ordered Ti nanodots with a radius of 30 nm and a height of 15 nm on a thin Ti layer as extracted from GISAXS and TEM measurements, which is in strong contrast with the formation of a mesoporous film. Notably, templates A and B have the same surface chemistry.

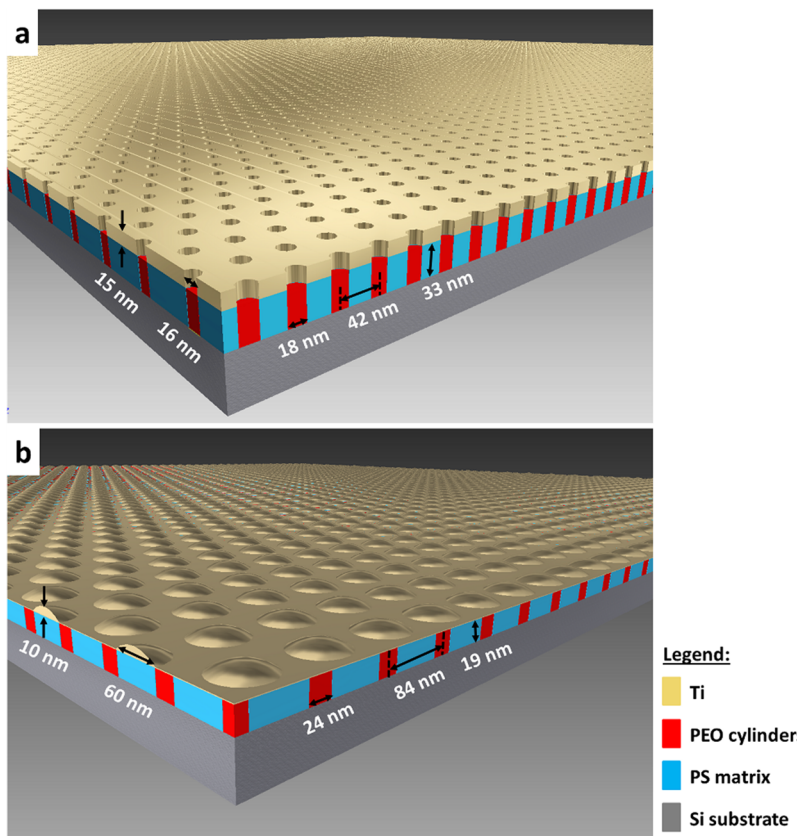


Figure 6. Schematics of (a) the mesoporous Ti film (sample C), and (b) the Ti nanodots on the corresponding microphase-separated BCP templates (sample D). The resulting dimensions are measured by GISAXS (Table 2) and XRR (Table 3).

Geometrical size and length scale commensurabilities indicate that Ti is PS-selective for both templates and deposits on the PS matrix between the PEO pores. The size of the nanodots ($d = 60 \text{ nm}$) is much larger than the PEO pore size ($d = 24 \text{ nm}$). The 60 nm nanodots fit in between the PEO pores with a center-to-center distance between the pores of 84 nm (Figure 6b). Therefore, also for the nanodot structure we deduce that Ti is PS-selective and deposits on the PS matrix surface in between the PEO pores. The affinity of evaporated metals to the PS part of a block copolymer sample has also been observed in a couple of different BCP/metal combinations.^{11,16,35} The affinity of Ti for one part of the block copolymer surface might be a result of the difference in surface energy of PS (36 mJ/m^2) and PEO (44 mJ/m^2).^{38,39}

These results imply that the Ti morphology depends not only on the surface chemistry of the template but also on the morphological critical dimensions of the template.

CONCLUSIONS

In conclusion, we demonstrate for the first time the differences of Ti aggregation on the different PS-*b*-PEO templates with different molecular weights. Evaporation of Ti on suitable BCP templates resulted in the formation of either Ti mesoporous films or nanoparticles with ordered hexagonal structures. The strong correlation between the critical dimensions of the BCP templates and the evolution of the Ti morphology was supported by GISAXS measurements. Both the underlying BCP template and the Ti structure were determined by GISAXS. A mesoporous Ti film formed on the smaller molecular weight BCP template (42 k–12 k), and hexagonally ordered Ti nanodots formed on the higher molecular weight

BCP template (102 k–34 k). X-ray scattering experiments confirmed a high substrate coverage, well-ordered packing of the BCP templates and coverage of the Ti coating over a large area. The combined use of GISAXS and XRR is critical for understanding the integration of titanium nanoparticles in PS–PEO polymer domains. These results demonstrate a method for directly obtaining mesoporous Ti films and ordered films of hexagonally packed Ti nanoparticles by only selecting an adequate BCP template.

METHODS

Materials and Sample Preparation. Silicon wafers were immersed in an ethanol bath for 1 h before rinsing with ultrapure water and drying under a stream of nitrogen. For template A, a 1% (w/w) solution of PS-*b*-PEO in toluene, which have average molecular masses of $M_{n,PS} = 42 \text{ kg/mol}$ and $M_{n,PEO} = 12 \text{ kg/mol}$ (42k–12 k), was spin coated onto silicon substrates at 3000 rpm for 60 s.

For template B, the silicon surfaces were functionalized by using polymer brushes. A 1% (w/w) solution of hydroxyl-terminated polystyrene in toluene was spin coated onto clean silicon wafers at 3000 rpm for 60 s before annealing for 3 h at 180 °C.⁴⁰ After rinsing the wafers with toluene to remove excess molecules, only the substrate-bound polymer brushes remained on the substrates. Afterward, a higher molecular mass PS-*b*-PEO with $M_{n,PS} = 102 \text{ kg/mol}$ and $M_{n,PEO} = 34 \text{ kg/mol}$ (102k–34 k) was dissolved in a 1% (w/w) toluene solution and spin coated onto silicon substrates at 3000 rpm for 60 s.

Finally, the titanium (Ti) was deposited on templates A and B by electron beam evaporation under a vacuum at a rate of 0.02 nm/sec until a nominal layer thickness of 10 nm was reached according to a quartz crystal microbalance calibration. For sample C, the Ti was deposited on template A ((42k–12k) + 10 nm Ti). For sample D, Ti was deposited on template B ((102k–34k) + 10 nm Ti).

Characterization. *Scanning Electron Microscopy (SEM).* SEM measurements were performed using an FEI Magellan 400L scanning electron microscope with an electron energy of 2 keV.

Transmission Electron Microscopy (TEM). TEM measurements were performed using an FEI Tecnai G² F20 transmission electron microscope. Cross sections of the measured samples were prepared by mechanical milling.

X-ray Photoelectron Spectroscopy (XPS). XPS measurements were performed at different angles with a Phoibos 150 analyzer (SPECS GmbH, Berlin, Germany) under ultrahigh vacuum conditions by using monochromatic Al K α radiation for the X-ray source with $\lambda = 8.34 \text{ \AA}$ (1486.74 eV).

X-ray Reflectometry (XRR). Information about the film structure with depth and density profile perpendicular to the sample surface (z -direction) was obtained from XRR measurements²¹ using a PANalytical XPert PRO reflectometer with monochromatic Cu K α radiation at a wavelength of $\lambda = 0.15 \text{ nm}$. The measurements were performed using a $\theta/2\theta$ geometry. A schematic of the setup is shown in the Supporting Information (Figure S1). All data were normalized for time and the incident beam intensity and are shown against the momentum transfer in the z -direction (Q_z) as follows:

$$Q_z = \frac{2\pi}{\lambda}(\sin \alpha_f + \sin \alpha_i) \quad (2)$$

where α_i and α_f are the incident and reflected beams, respectively. In addition, the condition for specular reflectivity $\alpha_i = \alpha_f$ was applied. The fits to the reflectivity data were performed by using the MOTOFIT software package (version 4, last modified at 12.11.2013),³² which is based on the Parratt formalism for calculating the reflectivity patterns of multilayer systems.⁴¹

Grazing-Incidence Small-Angle X-ray Scattering (GISAXS). The in-plane structures of the samples were investigated by using GISAXS measurements.²⁰ The measurements were conducted at the cSAXS beamline at the Swiss Light Source (Paul Scherrer Institute in Villigen, Switzerland) using monochromatic synchrotron radiation with a wavelength of $\lambda = 0.11 \text{ nm}$. The X-ray scattering patterns were recorded with a Pilatus 2M detector⁴² that was placed at a distance of 7465 mm from the sample with an evacuated flight tube between the sample and detector to reduce scattering and absorption due to air. Two beamstops were placed inside the flight tube to block the transmitted and specular beams. An additional vertical beamstop with a width of 1 mm was placed between the flight tube and the detector to block the elongated tails of the reflected beam. In some cases, this reflection was so strong that it caused a visible parasitic signal on the detector that resulted from the scattering of the flight tube exit window (as shown in Figure 2a,b by the white circular arcs). The entire area that was covered by the beamstops is marked with a vertical gray bar in all of the data shown in Figure 2. In addition, dark horizontal and vertical lines can be observed due to the gaps between the Pilatus detector modules.⁴² The samples were mounted on a hexapod and were measured under an incident angle of $\alpha_i = 0.25^\circ$, which is above the critical angle of the polymer film ($\alpha_c(\text{PS-PEO}) \approx 0.14^\circ$) and the silicon substrate ($\alpha_c(\text{Si}) = 0.16^\circ$).^{22,25,35} Therefore, this selected angle allows for the detection of the characteristic Yoneda wings and the specular reflectivity peak on well-separated positions on the 2D detector.³⁴ The X-ray beam had a width of 400 μm in the horizontal direction and 150 μm in the vertical direction, which allowed the entire length of the sample (20 mm) along the beam direction to be probed due to the small incidence angle. Overall, an area of 8 mm^2 was probed. To avoid beam damage, 150 acquisitions were measured for all samples with exposure times of 0.2 s for each acquisition. All frames were averaged after verifying that no detectable radiation damage occurred. The intensity plots are shown as a function of the momentum transfer in the y - and z -directions (Q_y and Q_z). The Q_z vector is given by eq 2 with the incident and exit vertical angles (α_i and α_f). The Q_y vector is given by

$$Q_y = \frac{2\pi}{\lambda} \sin \theta \cos \alpha_f \quad (3)$$

where the exit horizontal angle θ is illustrated in the Supporting Information (Figure S1). For structural analysis, Q_y cuts were made parallel to the sample surface at the Q_z positions with maximum intensities. All cuts were integrated over a finite Q_z range to improve statistics. The line cuts were fit using the IsGISAXS software package (version 2.6).²³ The results were evaluated within the distorted-wave Born approximation (DWBA) by considering multiple scattering effects and 2D GISAXS maps were simulated using the same software.

ASSOCIATED CONTENT

S Supporting Information

Schematic diagram of the XRR and GISAXS geometry. This material is available free of charge via the Internet at <http://pubs.acs.org>.

AUTHOR INFORMATION

Corresponding Author

*(M.K.) E-mail: martin.kreuzer@icn.cat.

Notes

The authors declare no competing financial interest.

ACKNOWLEDGMENTS

The authors acknowledge financial support from the EU-FP7 Integrated Infrastructure Initiative No. 262348 from the European Soft Matter Infrastructure (ESMI), LAMAND (Grant No. 245565), MERGING (Grant No. 309150), the Spanish MINECO project TAPHOR (MAT2012-31392), and the Deutsche Forschungsgemeinschaft (Grant No. KR 4522/1-1). In addition, we thank X. Donath for technical assistance, J. Andreasen and M. Guizar-Sicairos for their help during the GISAXS measurements, and A. Menzel for carefully reading the manuscript. Furthermore, the authors thank B. Ballesteros, M. Rosado, and F. J. Belarre for the SEM and TEM measurements and G. Sauthier and P. García for the XPS and XRR measurements.

REFERENCES

- (1) Devan, R. S.; Patil, R. A.; Lin, J.-H.; Ma, Y.-R. One-Dimensional Metal-Oxide Nanostructures: Recent Developments in Synthesis, Characterization, and Applications. *Adv. Funct. Mater.* **2012**, 22 (16), 3326–3370 <http://dx.doi.org/10.1002/adfm.201201008>.
- (2) Rignanese, G.-M. Dielectric properties of crystalline and amorphous transition metal oxides and silicates as potential high- κ candidates: the contribution of density-functional theory. *J. Phys.: Condens. Matter* **2005**, 17 (7), R357 <http://dx.doi.org/10.1088/0953-8984/17/7/R03>.
- (3) Emeline, A. V.; Kataeva, G. V.; Panasuk, A. V.; Ryabchuk, V. K.; Sheremeteva, N. V.; Serpone, N. Effect of Surface Photoreactions on the Photocoloration of a Wide Band Gap Metal Oxide: Probing Whether Surface Reactions Are Photocatalytic. *J. Phys. Chem. B* **2005**, 109 (11), 5175–5185 <http://dx.doi.org/10.1021/jp0452047>.
- (4) Haruta, M.; Daté, M. Advances in the catalysis of Au nanoparticles. *Appl. Catal. A: Gen.* **2001**, 222 (1–2), 427–437 [http://dx.doi.org/10.1016/S0926-860X\(01\)00847-X](http://dx.doi.org/10.1016/S0926-860X(01)00847-X).
- (5) Arpi, M.; Subhayan, B.; Faruk, H. M.; Takakazu, T. Study of gradual variation of structural, surface morphological and photocatalytic properties of sol-gel derived transparent TiO₂ thin film. *J. Phys.: Conf. Ser.* **2008**, 100 (1), 012006 <http://dx.doi.org/10.1088/1742-6596/100/1/012006>.
- (6) Simão, C.; Khunsin, W.; Kehagias, N.; Salaun, M.; Zelmann, M.; Morris, M. A.; Torres, C. M. S. Order quantification of hexagonal periodic arrays fabricated by *in situ* solvent-assisted nanoimprint lithography of block copolymers. *Nanotechnology* **2014**, 25 (17), 175703 <http://dx.doi.org/10.1088/0957-4484/25/17/175703>.
- (7) Shin, K.; Leach, K. A.; Goldbach, J. T.; Kim, D. H.; Jho, J. Y.; Tuominen, M.; Hawker, C. J.; Russell, T. P. A Simple Route to Metal

- Nanodots and Nanoporous Metal Films. *Nano Lett.* **2002**, *2* (9), 933–936 <http://dx.doi.org/10.1021/nl0256560>.
- (8) Park, M.; Chaikin, P. M.; Register, R. A.; Adamson, D. H. Large area dense nanoscale patterning of arbitrary surfaces. *Appl. Phys. Lett.* **2001**, *79* (2), 257–259 <http://dx.doi.org/10.1063/1.1378046>.
- (9) Aizawa, M.; Buriak, J. M. Block Copolymer Templated Chemistry for the Formation of Metallic Nanoparticle Arrays on Semiconductor Surfaces. *Chem. Mater.* **2007**, *19* (21), 5090–5101 <http://dx.doi.org/10.1021/cm071382b>.
- (10) Yun, H. S.; Miyazawa, K.; Zhou, H. S.; Honma, I.; Kuwabara, M. Synthesis of Mesoporous Thin TiO₂ Films with Hexagonal Pore Structures Using Triblock Copolymer Templates. *Adv. Mater.* **2001**, *13* (18), 1377–1380 <http://onlinelibrary.wiley.com/doi/10.1002/1521-4095%28200109%2913:18%3C1377::AID-ADMA1377%3E3.0.CO;2-T/abstract>.
- (11) Lopes, W. A. Nonequilibrium self-assembly of metals on diblock copolymer templates. *Phys. Rev. E* **2002**, *65* (3), 21 <http://dx.doi.org/10.1103/PhysRevE.65.031606>.
- (12) Lee, W.; Lee, S. Y.; Zhang, X.; Rabin, O.; Briber, R. M. Hexagonally ordered nanoparticles templated using a block copolymer film through Coulombic interactions. *Nanotechnology* **2013**, *24* (4), 045305 <http://dx.doi.org/10.1088/0957-4484/24/4/045305>.
- (13) Ghoshal, T.; Maity, T.; Senthamarai Kannan, R.; Shaw, M. T.; Carolan, P.; Holmes, J. D.; Roy, S.; Morris, M. A. Size and space controlled hexagonal arrays of superparamagnetic iron oxide nanodots: magnetic studies and application. *Sci. Rep.* **2013**, *3* (2772), 1–8 <http://dx.doi.org/10.1038/srep02772>.
- (14) Park, S.; Wang, J.-Y.; Kim, B.; Xu, J.; Russell, T. P. A Simple Route to Highly Oriented and Ordered Nanoporous Block Copolymer Templates. *ACS Nano* **2008**, *2* (4), 766–772 <http://dx.doi.org/10.1021/nn7004415>.
- (15) Kim, D. H.; Kim, S. H.; Lavery, K.; Russell, T. P. Inorganic Nanodots from Thin Films of Block Copolymers. *Nano Lett.* **2004**, *4* (10), 1841–1844 <http://dx.doi.org/10.1021/nl049063w>.
- (16) Lopes, W. A.; Jaeger, H. M. Hierarchical self-assembly of metal nanostructures on diblock copolymer scaffolds. *Nature* **2001**, *414* (6865), 735–738 <http://dx.doi.org/10.1038/414735a>.
- (17) Zou, W.; Cai, X.; Li, J.; Dai, X.; Zhang, H.; Zhou, A.; Li, J.; Song, L.; Iyoda, T. Selective deposition on block copolymer film by thermal evaporation of silver. *Surf. Coat. Technol.* **2012**, *26* (22), 4634–4638 <http://dx.doi.org/10.1016/j.surfcoat.2012.05.028>.
- (18) Morkved, T. L.; Wiltzius, P.; Jaeger, H. M.; Grier, D. G.; Witten, T. A. Mesoscopic self-assembly of gold islands on diblock-copolymer films. *Appl. Phys. Lett.* **1994**, *64* (4), 422–424 <http://dx.doi.org/10.1063/1.111118>.
- (19) Tadd, E. H.; Bradley, J.; Tannenbaum, R. Spatial Distribution of Cobalt Nanoclusters in Block Copolymers. *Langmuir* **2002**, *18* (6), 2378–2384 <http://dx.doi.org/10.1021/la011108a>.
- (20) Müller-Buschbaum, P. Grazing incidence small-angle X-ray scattering: an advanced scattering technique for the investigation of nanostructured polymer films. *Anal. Bioanal. Chem.* **2003**, *376* (1), 3–10 <http://dx.doi.org/10.1007/s00216-003-1869-2>.
- (21) Prins, J. A. The Total Reflection of X-Rays. *Nature* **1927**, *120*, 188–189 <http://dx.doi.org/10.1038/120188a0>.
- (22) Metwalli, E.; Körstgens, V.; Schrage, K.; Meier, R.; Kaune, G.; Buffet, A.; Couet, S.; Roth, S. V.; Röhrsberger, R.; Müller-Buschbaum, P. Cobalt Nanoparticles Growth on a Block Copolymer Thin Film: A Time-Resolved GISAXS Study. *Langmuir* **2013**, *29* (21), 6331–6340 <http://dx.doi.org/10.1021/la400741b>.
- (23) Lazzari, R. IsGISAXS: a program for grazing-incidence small-angle X-ray scattering analysis of supported islands. *J. Appl. Crystallogr.* **2002**, *35* (4), 406–421 <http://dx.doi.org/10.1107/S0021889802006088>.
- (24) Yokoyama, H. Small angle X-ray scattering studies of nanocellular and nanoporous structures. *Polym. J.* **2013**, *45* (1), 3–9 <http://dx.doi.org/10.1038/pj.2012.205>.
- (25) Sinha, S. K.; Sirota, E. B.; Garoff, S.; Stanley, H. B. X-ray and neutron scattering from rough surfaces. *Phys. Rev. B* **1988**, *38* (4), 2297–2311 <http://dx.doi.org/10.1103/PhysRevB.38.2297>.
- (26) Bolze, J.; Ree, M.; Youn, H. S.; Chu, S.-H.; Char, K. Synchrotron X-ray Reflectivity Study on the Structure of Templatized Polyorganosilicate Thin Films and Their Derived Nanoporous Analogs. *Langmuir* **2001**, *17* (21), 6683–6691 <http://dx.doi.org/10.1021/la010451c>.
- (27) Kim, T.; Wooh, S.; Son, J. G.; Char, K. Orientation Control of Block Copolymer Thin Films Placed on Ordered Nanoparticle Monolayers. *Macromolecules* **2013**, *46* (20), 8144–8151 <http://dx.doi.org/10.1021/ma401601f>.
- (28) Yao, L.; Woll, A. R.; Watkins, J. J. Directed Assembly of Block Copolymer Templates for the Fabrication of Mesoporous Silica Films with Controlled Architectures via 3-D Replication. *Macromolecules* **2013**, *46* (15), 6132–6144 <http://dx.doi.org/10.1021/ma401018y>.
- (29) Pitet, L. M.; Wuister, S. F.; Peeters, E.; Kramer, E. J.; Hawker, C. J.; Meijer, E. W. Well-Organized Dense Arrays of Nanodomains in Thin Films of Poly(dimethylsiloxane)-b-poly(lactide) Diblock Copolymers. *Macromolecules* **2013**, *46* (20), 8289–8295 <http://dx.doi.org/10.1021/ma401719p>.
- (30) Wu, H.; Huang, X. Structural Evolution of Low-Molecular-Weight Poly(ethylene oxide)-block-polystyrene Diblock Copolymer Thin Film. *Sci. World J.* **2013**, *2013*, 7 <http://dx.doi.org/10.1155/2013/539457>.
- (31) Mutter, R.; Strobl, G.; Stühn, B. Structure of thin block copolymer films studied by X-ray reflectivity. *Fresenius' J. Anal. Chem.* **1993**, *346* (1–3), 297–299 <http://dx.doi.org/10.1007/BF00321435>.
- (32) Nelson, A. Co-refinement of multiple-contrast neutron/X-ray reflectivity data using MOTOFIT. *J. Appl. Crystallogr.* **2006**, *39* (2), 273–276 <http://dx.doi.org/10.1107/S0021889806005073>.
- (33) Golub, M.; Lott, D.; Watkins, E.; Garamus, V.; Lüthringher, B.; Stoermer, M.; Schreyer, A.; Willumeit, R. X-ray and neutron investigation of self-assembled lipid layers on a titanium surface. *Biointerphases* **2013**, *8* (1), 21 <http://dx.doi.org/10.1186/1559-4106-8-21>.
- (34) Yoneda, Y. Anomalous Surface Reflection of X Rays. *Phys. Rev.* **1963**, *131* (5), 2010–2013 <http://dx.doi.org/10.1103/PhysRev.131.2010>.
- (35) Metwalli, E.; Couet, S.; Schrage, K.; Rohlsberger, R.; Körstgens, V.; Ruderer, M.; Wang, W.; Kaune, G.; Roth, S. V.; Müller-Buschbaum, P. In situ GISAXS Investigation of Gold Sputtering onto a Polymer Template. *Langmuir* **2008**, *24* (8), 4265–4272 <http://dx.doi.org/10.1021/la7038587>.
- (36) Kreuzer, M.; Strobl, M.; Reinhardt, M.; Hemmer, M. C.; Hauß, T.; Dahint, R.; Steitz, R. Impact of a model synovial fluid on supported lipid membranes. *Biochim. Biophys. Acta (BBA)* **2012**, *1818* (11), 2648–2659 <http://dx.doi.org/10.1016/j.bbamem.2012.05.022>.
- (37) Cai, K.; Müller, M.; Bossert, J.; Rechtenbach, A.; Jandt, K. D. Surface structure and composition of flat titanium thin films as a function of film thickness and evaporation rate. *Appl. Surf. Sci.* **2005**, *250* (1–4), 252–267 <http://dx.doi.org/10.1016/j.apsusc.2005.01.013>.
- (38) Neto, C.; James, M.; Telford, A. M. On the Composition of the Top Layer of Microphase Separated Thin PS-PEO Films. *Macromolecules* **2009**, *42* (13), 4801–4808 <http://dx.doi.org/10.1021/mg900690e>.
- (39) Zhang, L.; Zeng, H.; Liu, Q. Probing Molecular and Surface Interactions of Comb-Type Polymer Polystyrene-graft-poly(ethylene oxide) (PS-g-PEO) with an SFA. *J. Phys. Chem. C* **2012**, *116* (33), 17554–17562 <http://dx.doi.org/10.1021/jp303561p>.
- (40) Ji, S.; Liu, G.; Zheng, F.; Craig, G. S. W.; Himpel, F. J.; Nealey, P. F. Preparation of Neutral Wetting Brushes for Block Copolymer Films from Homopolymer Blends. *Adv. Mater.* **2008**, *20* (16), 3054–3060 <http://dx.doi.org/10.1002/adma.200800048>.
- (41) Parratt, L. G. Surface Studies of Solids by Total Reflection of X-Rays. *Phys. Rev.* **1954**, *95* (2), 359 <http://dx.doi.org/10.1103/PhysRev.95.359>.
- (42) Kraft, P.; Bergamaschi, A.; Bronnimann, C.; Dinapoli, R.; Eikenberry, E. F.; Graafsmo, H.; Henrich, B.; Johnson, I.; Kobas, M.; Mozzanica, A.; Schleputz, C. M.; Schmitt, B. Characterization and Calibration of PILATUS Detectors. *IEEE Trans. Nucl. Sci.* **2009**, *56* (3), 758–764 <http://dx.doi.org/10.1109/tns.2008.2009448>.